Electrochimica Acta 247 (2017) 1019–1029

Contents lists available at ScienceDirect

Electrochimica Acta

journal homepage: www.elsevier.com/locate/electacta

Cathodic over-potential and hydrogen partial pressure coupling in hydrogen evolution reaction of marine steel under hydrostatic pressure

X.L. Xiong[a], Q.J. Zhou[b], J.X. Li[a], Alex A. Volinsky[c], Y.J. Su[a,*]

[a] Corrosion and Protection Center, Key Laboratory for Environmental Fracture (MOE), University of Science and Technology Beijing, Beijing 100083, China
[b] Research Institute, Baoshan Iron & Steel Co. Ltd, Shanghai 201900, China
[c] Department of Mechanical Engineering, University of South Florida, Tampa FL 33620, USA

ARTICLE INFO

Article history:
Received 14 February 2017
Received in revised form 9 June 2017
Accepted 11 June 2017
Available online 12 June 2017

Keywords:
Hydrogen evolution
Hydrostatic pressure
Electrochemical impedance
Kinetic parameters
Surface coverage

ABSTRACT

A new electrochemical impedance spectroscopy (EIS) model, which considers both the Tafel recombination and the Heyrovsky reaction under permeable boundary conditions, was developed to characterize the kinetic parameters of the hydrogen evolution reaction (HER) under hydrostatic pressure. The effect of the hydrostatic pressure on the kinetic parameters of the HER and the permeation of A514 steel in alkaline solution were measured using potentiodynamic polarization, the Devanathan cell hydrogen permeation, and EIS. The hydrostatic pressure accelerates the Volmer reaction and inhibits the Tafel recombination, which increases the number of adsorbed hydrogen atoms. On the other hand, the pressure accelerates the Heyrovsky reaction, which decreases the amount of adsorbed hydrogen atoms. At 10 to 40 MPa hydrostatic pressure within the −1.0 to −1.1 V_{SSE} cathodic potential region, the HER is controlled by hydrogen partial pressure, and hydrogen adsorption is the Langmuir type. Within the −1.2 to −1.3 V_{SSE} cathodic potential region, the HER is controlled by the potential, and hydrogen adsorption gradually transfers from the Langmuir type to the Temkin type with increasing hydrostatic pressure.

1. Introduction

The criteria for the cathodic protection of structural steel under deep sea water have been widely discussed in recent decades [1–4]. These factors have been studied because hydrostatic pressure is one of the environmental factors in deep sea water that changes the behavior of the hydrogen evolution reaction (HER) and hydrogen permeation in metal, which can induce severe hydrogen-induced cracking (HIC) of metallic materials and structures [5,6]. Olsen and Hesjevik proved that hydrostatic pressure could significantly increase hydrogen concentration in super martensitic stainless and duplex stainless steels when immersed in 3.5% NaCl electrolyte with aluminum anodes, which reveals that HIC occurs more easily in deep sea environment [7]. This stimulates the study of the pressure effect on HER and permeation in metals.

By using the Devanathan cell hydrogen permeation [8], Nanis and DeLuccia [9], Woodward and Procter [10] claimed that the steady-state current density increases with hydrostatic pressure, while Blundy and Shreir [11], Smirnova and Johnsen [12] indicated that the steady-state current density was independent of the hydrostatic pressure when stirring electrolyte in a hydrogen charging cell during permeation. These results indicate that the surface effects, including the HER, dominate the pressure effect on hydrogen interaction with metal. Our previous work considered the surface effect on the hydrogen entry side. Based on the surface effect model [13], it was found that hydrogen concentration on the subsurface of the A514 steel membrane increased with hydrostatic pressure [14]. However, the effects of the hydrostatic pressure on kinetic parameters of the HER still remain unclear, which is the key factor that should be considered in the cathodic protection criteria under deep sea water.

The process of the HER of iron or steel in alkaline solution, which is believed to be an indirect model, is shown by the following steps [15–17].

$$H_2O + M + e^- \underset{k_a}{\overset{k_1}{\rightleftarrows}} MH_{ads} + OH^- \quad (1)$$

Reaction (1) is the Volmer reaction, where M is the electrode, *e.g.* iron or steel and MH_{ads} is the adsorbed hydrogen atom on the surface of the electrode. The second step is known as the Heyrovsky reaction:

$$MH_{ads} + H_2O + e^- \overset{k_2}{} H_2 + OH^- + M \quad (2)$$

* Corresponding author.
E-mail address: yjsu@ustb.edu.cn (Y.J. Su).

http://dx.doi.org/10.1016/j.electacta.2017.06.063
0013-4686/

The Heyrovsky reaction is coupled with the Tafel recombination:

$$MH_{ads} + MH_{ads} \xrightarrow{k_3} H_2 + 2M \quad (3)$$

A part of the adsorbed hydrogen atoms diffuse into the subsurface just below the electrode surface and become absorbed hydrogen atoms:

$$MH_{ads} + M_{subsurface} \underset{k_{-4}}{\overset{k_4}{\rightleftarrows}} M_{surface} + MH_{abs}(subsurface) \quad (4)$$

The next step is the bulk diffusion of the absorbed hydrogen atoms:

$$MH_{abs}(subsurface) \xrightarrow{diffusion} MH_{abs}(bulk) \quad (5)$$

On the other hand, the direct hydrogen entry model claimed that hydrogen atoms diffuse into bulk metal without the adsorbed state [18,19]. The direct model is suitable for metals in the acidic solutions, or metals with weak hydrogen evolution and strong hydrogen absorption reaction [19].

An approach to measure kinetic parameters of the HER based on the analysis of electrochemical impedance spectra (EIS) in the double Devanathan cell has been mentioned by a few researchers [20–22]. The theoretical analysis of EIS on the HER for both direct and indirect models was carried out by Lim and Pyun, who considered palladium [20,23]. However, these models have only considered metals with strong hydrogen absorption reaction. Thus, reaction (2) has been ignored in their simplified mathematical model. For the iron/hydrogen system, especially in alkaline solutions, both the Tafel recombination and the Heyrovsky reaction should be considered [24]. Even though numerous studies have been performed [21,22,25], many problems remain to be solved. Additionally, few research studies have been performed by using impedance measurements due to the complexity of the mathematical description of the EIS model. However, EIS is a useful method to distinguish each process contained in the multi-step reaction.

In this work, the abnormal phenomenon of potentiodynamic polarization in the −0.8 to $-1.1\ V_{SSE}$ potential region and 10 to 40 MPa pressure region is reported, *i.e.*, the current density decreases with decreasing cathodic potential (decreasing cathodic potential means that the potential is more negative). Potentiostatic hydrogen permeation and EIS analysis on the hydrogen entry side under steady boundary conditions at different hydrostatic pressure were performed. A new EIS model, which considered both the Tafel recombination and the Heyrovsky reaction under permeation boundary conditions was developed to extract kinetic parameters of the HER from the EIS experimental data. Potentiodynamic polarization and hydrogen permeation results combined with the EIS analysis at various pressures were discussed with the aim of demonstrating hydrostatic pressure effects on kinetic parameters of the HER.

2. Experimental

2.1. Test material

A514 offshore structural steel is adopted in this research. The material composition is as follows (wt.%): 0.2C, 0.78 Mn, 0.49 Cr, 0.20 Mo, 0.049 V, 0.0006 B, 0.008 P, 0.006 S, and 0.02 Ti. The hydrogen permeation samples are circular with 1.2 cm diameter and 0.5 mm thicknesses within a measurement error of 0.01 mm. Thus, the edge effects are minimized to assure the applicability of the one-dimensional model. Both sides of the specimens were polished with 360 and 1500 grit sandpaper followed by polishing cloth using automatic polishing machine. One side of each specimen was coated with 100 nm of nickel using a thin film sputtering system (LAD18, KJLC).

2.2. Test equipment

The hydrostatic pressure equipment consists of a two compartment autoclave integrated with a hydraulic system and a temperature control system, as shown in previous work [14]. Temperature in the autoclaves can be controlled in the 0–40 °C range. The electrolyte in the autoclaves can be pressurized to a maximum hydrostatic pressure of 56 MPa with a solution supplied from an external tank.

2.3. Electrochemical characterization

Potentiodynamic polarization tests, along with hydrogen permeation and EIS measurements were conducted using the hydrostatic pressure equipment with a three electrode system. Platinum foil with 10 mm × 30 mm size was used as the counter electrode and the Ag/AgCl electrode (SSE) saturated with KCl was used as the reference electrode (0.65 V *vs* RHE). The test pressure ranged from 0.1 to 40 MPa (equivalent to the hydrostatic pressure at 4000 m depth in the ocean). In addition, the electrochemical experiments were performed in 0.2 mol/L NaOH solution in both cells.

Constant cathodic potential varied from −1.0 to $-1.3\ V_{SSE}$ was applied to the specimens in the hydrogen charging cell during hydrogen permeation test. Hydrogen atoms were produced and adsorbed onto the specimen surfaces, some of which became absorbed and diffused into the material. In the other cell (oxidation cell), a positive +300 mV_{SSE} overvoltage was applied to the opposite surface of the specimen. Hydrogen reaching the surface via diffusion through the specimen was immediately oxidized, and hydrogen current was measured.

Traps significantly affect hydrogen diffusivity in metals [26–28]. In particular, Kim et al. noted that the trap density during the first permeation was twice higher than during the second permeation [29]. To assure the reliability and repeatability of the experiment, hydrogen charging was carried out first to fill the traps under atmospheric pressure, and then, all of the charged specimens were exposed to air for 48 hours to completely release diffusible hydrogen atoms from the lattice. The hydrogen permeation experiments were then performed under different hydrostatic pressure.

EIS measurements were performed on the hydrogen entry side after hydrogen permeation attained steady state using the Gamry Interface 1000 tool. An AC signal with an amplitude of 10 mV was applied at a DC potential varied from −1.0 to $-1.3\ V_{SSE}$. The frequency was varied from 0.01 to 10^5 Hz. After the open circuit potential stabilized, the potentiodynamic polarization test was performed with the potential ranged from −0.1 to $-1.3\ V_{SSE}$ at a scanning rate of 0.33 mV/s. All electrochemical experiments were carried out at 25 °C.

3. Theory

Based on the second Fick's law, hydrogen flux, $J_x = 0$, under sinusoidal oscillating voltage boundary conditions was reported by Lim and Pyun [23].

$$J_{x=0} = \frac{D}{l}C_0 + \sqrt{j\omega D}\coth\left(\sqrt{\frac{j\omega}{D}}l\right)\tilde{C_0}\exp(j\omega t) \quad (6)$$

Where D is the intrinsic diffusivity of hydrogen in bulk metal, l is the specimens' thickness, C_0 is the hydrogen concentration on the entry side at steady state, $\tilde{C_0}$ is the perturbation of the hydrogen

concentration on the entry side of the specimens, ω is the angular frequency, j is a complex number, and t is time. The subscript $x = 0$ means the hydrogen entry side of the membrane.

Lim's model considered the process where hydrogen atoms passed through the surface to the subsurface of the specimens. This process is shown as reactions (1), (3), (4) and (5). This model is mainly focused on HER of Pd. The fast discharge and slow recombination mechanism, proposed by many authors [30,31], has dominated the HER on Pd. Therefore, the Heyrovsky reaction (2) was not considered in these models. However, during hydrogen evolution from iron in alkaline solution [24], the Heyrowsky reaction is significant and can't be ignored.

Taking the Heyrovsky reaction into account, the part of the Faradaic admittance at steady state involving the HER and the hydrogen adsorption reaction (HAR) can be derived as follows:

$$-\frac{i_f}{F} = v_1 + v_2 \tag{7}$$

and

$$\Gamma_{\max}\frac{d\theta}{dt} = v_1 - v_2 - 2v_3 - J_{x=0} \tag{8}$$

Where F is the Faraday constant, i_f is the Faradaic current, θ is the H_{ads} surface coverage, $\Gamma_{\max}$ is the saturation value of the surface hydrogen concentration, and v_i ($i = 1, 2, 3$) is the reaction rate of reactions (1) to (3).

The effect of the potential oscillation on the reactions (1)–(4) can be represented by the Taylor series expansion. Under the reaction constraints and neglecting the second and higher responses, the reaction rates from the reactions (1)–(4) are given as

$$v_1 = v_1^{ss} + \left(\frac{\partial v_1}{\partial E}\right)\tilde{E}\exp(j\omega) + \left(\frac{\partial v_1}{\partial \theta}\right)\tilde{\theta}\exp(j\omega) \tag{9}$$

$$v_2 = v_2^{ss} + \left(\frac{\partial v_2}{\partial E}\right)\tilde{E}\exp(j\omega) + \left(\frac{\partial v_2}{\partial \theta}\right)\tilde{\theta}\exp(j\omega) \tag{10}$$

$$v_3 = v_3^{ss} + \left(\frac{\partial v_3}{\partial \theta}\right)\tilde{\theta}\exp(j\omega) \tag{11}$$

$$v_4 = v_4^{ss} + \left(\frac{\partial v_4}{\partial \theta}\right)\tilde{\theta}\exp(j\omega) + \left(\frac{\partial v_4}{\partial C_s}\right)\tilde{C}_0\exp(j\omega) \tag{12}$$

Where v_i^{ss} is the steady state reaction rate of the reaction (i), and v_4 is the reaction rate of the reaction (4). Assuming that hydrogen surface coverage is small, the rate of the reaction (4) is mentioned by many investigations as in [23,24]:

$$v_4 = k_4\theta - k_{-4}C_0 \tag{13}$$

Where k_4 and k_{-4} are the kinetic parameters of the forward and reverse reaction (4). Substituting Eqs. (6) and (9) into Eqs. (12),(7) and (8), the alternating current part can be written as

$$-\frac{\tilde{i}_f}{F} = \left(\frac{\partial v_1}{\partial E}\right)\tilde{E} + \left(\frac{\partial v_1}{\partial \theta}\right)\tilde{\theta} + \left(\frac{\partial v_2}{\partial E}\right)\tilde{E} + \left(\frac{\partial v_2}{\partial \theta}\right)\tilde{\theta} \tag{14}$$

$$\begin{aligned} j\omega\Gamma_{\max}\tilde{\theta} = {} & \left(\frac{\partial v_1}{\partial E}\right)\tilde{E} + \left(\frac{\partial v_1}{\partial \theta}\right)\tilde{\theta} - \left(\frac{\partial v_2}{\partial E}\right)\tilde{E} - \left(\frac{\partial v_2}{\partial \theta}\right)\tilde{\theta} \\ & - 2\left(\frac{\partial v_3}{\partial \theta}\right)\tilde{\theta} - \sqrt{j\omega D}\coth\left(\sqrt{\frac{j\omega}{D}}L\right)\tilde{C}_0 \end{aligned} \tag{15}$$

Based on the AC conditions, one obtains

$$J_{x=0} = v_4 \tag{16}$$

Thus, by substituting Eqs. (6) and (12) into Eq. (16), one obtains

$$\frac{\tilde{C}_0}{\tilde{\theta}} = \frac{\left(\frac{\partial v_4}{\partial \theta}\right)}{-\left(\frac{\partial v_4}{\partial C_s}\right) + \sqrt{j\omega D}\coth\left(\sqrt{\frac{j\omega}{D}}L\right)\tilde{C}_0} \tag{17}$$

Combining Eqs. (14), (15) and (17), the Faradaic admittance Y_f is determined as

$$\begin{aligned} Y_f = \frac{\tilde{i}_f}{\tilde{E}} & = -F\left[\left(\frac{\partial v_1}{\partial E}\right) + \left(\frac{\partial v_2}{\partial E}\right)\right] \\ & - F\frac{\left[\left(\frac{\partial v_1}{\partial E}\right) - \left(\frac{\partial v_2}{\partial E}\right)\right]\left[\left(\frac{\partial v_1}{\partial \theta}\right) + \left(\frac{\partial v_2}{\partial \theta}\right)\right]}{j\omega\Gamma_{\max} - \left[\left(\frac{\partial v_1}{\partial \theta}\right) - \left(\frac{\partial v_2}{\partial \theta}\right)\right] + 2\left(\frac{\partial v_3}{\partial \theta}\right) + \frac{\left(\frac{\partial v_4}{\partial \theta}\right)}{1 - \frac{\left(\frac{\partial v_4}{\partial C_0}\right)}{\sqrt{j\omega D}\coth\left(\sqrt{\frac{j\omega}{D}}L\right)}}} \end{aligned} \tag{18}$$

Many researches reported that only a small fraction of the adsorbed hydrogen may diffuse into the metal lattice in the case of iron and steel [21,32]. Thus, reactions (4) and (5) can be reasonably ignored. The Faradaic admittance can be simplified as

$$\begin{aligned} Y_f = \frac{\tilde{i}_f}{\tilde{E}} & = -F\left[\left(\frac{\partial v_1}{\partial E}\right) + \left(\frac{\partial v_2}{\partial E}\right)\right] \\ & - F\frac{\left[\left(\frac{\partial v_1}{\partial E}\right) - \left(\frac{\partial v_2}{\partial E}\right)\right]\left[\left(\frac{\partial v_1}{\partial \theta}\right) + \left(\frac{\partial v_2}{\partial \theta}\right)\right]}{j\omega\Gamma_{\max} - \left[\left(\frac{\partial v_1}{\partial \theta}\right) - \left(\frac{\partial v_2}{\partial \theta}\right)\right] + 2\left(\frac{\partial v_3}{\partial \theta}\right)} \end{aligned} \tag{19}$$

This model can reveal the HER, including both the Tafel recombination and the Heyrovsky reactions. The simplified model is similar to the Bai's model [15]:

$$\frac{1}{R_{ct}} = -F\left[\left(\frac{\partial v_1}{\partial E}\right) + \left(\frac{\partial v_2}{\partial E}\right)\right] \tag{20}$$

$$\frac{1}{R_0} = -\frac{F}{\Gamma_{\max}}\left[\left(\frac{\partial v_1}{\partial E}\right) - \left(\frac{\partial v_2}{\partial E}\right)\right]\left[\left(\frac{\partial v_1}{\partial \Gamma}\right) + \left(\frac{\partial v_2}{\partial \Gamma}\right)\right]\tau \tag{21}$$

$$\frac{1}{\tau} = \frac{1}{\Gamma_{\max}}\left\{2\left(\frac{\partial v_3}{\partial \Gamma}\right) - \left[\left(\frac{\partial v_1}{\partial \Gamma}\right) - \left(\frac{\partial v_2}{\partial \Gamma}\right)\right]\right\} \tag{22}$$

$$C_{ad} = -\frac{R_0}{R_{ct}^2}\tau \tag{23}$$

$$R_{ev} = \left(-\frac{R_0}{R_{ct}^2} - \frac{1}{R_{ct}}\right)^{-1} \tag{24}$$

Eq. (19), which represents the Faradaic admittance, is expressed as the impedance equation and the electrical equivalent circuit, as shown in Eq. (25) and Fig. 1. Here, R_s is the resistance of the electrolyte, R_{ct} is the charging transfer resistance, C_{dl} is the double layer capacitance, C_{ad} is the pseudo-capacitance, R_{ev} is related to the HER, and R_0 and τ are the additional resistance at zero frequency and the relaxation time, respectively. These variables are defined based on the Armstrong's theory and used to represent the

Faradaic impedance, Z_f, in equation (25) [33].

$$Z_f = R_{ct} + \frac{1}{j\omega C_{ad} + \frac{1}{R_{ev}}} \tag{25}$$

4. Results

4.1. Potentiodynamic polarization measurements

The potentiodynamic polarization curves presented in Fig. 2 were measured at different hydrostatic pressures. The equilibrium potential increases with hydrostatic pressure, which agrees with other experimental results, where the equilibrium potential of 316L stainless steel in 3.5% NaCl increases with hydrostatic pressure [34]. Sarkar and Aquino put forward a model based on the Butler–Volmer equation [35]. The theoretical analysis also showed that the effect of compressive stress can inhibit the anodic reaction and increase the cathodic reaction rate [36]. However, it is quite small compared with the influence of hydrostatic pressure on HER. Thus, we ignored the effect of the electrode electrochemical properties change induced by compressive stress (hydrostatic pressure) on HER, and focused on the effect of hydrostatic pressure on the HER itself.

The relationship between the cathodic potential and the current in the Tafel linear area can be described as

$$\eta_c = -\frac{2.3RT}{(1-\alpha)F}\log j^0 + \frac{2.3RT}{\alpha F}\log j_c \tag{26}$$

Where η_c is the cathodic over potential ($\eta_c = E - E_{eq}$,E_{eq} is the equilibrium potential, E is the cathodic potential), j_c is the cathodic current density, and α is the transfer coefficient, j° is the exchange current density. The parameters obtained from Fig. 2 are listed in Table 1.

As shown in Table 1, both the equilibrium potential and current increase with the hydrostatic pressure. On the other hand, the Tafel slope on the cathodic side decreases with hydrostatic pressure. Based on Eq. (26), the transfer coefficients can be obtained, which increase with hydrostatic pressure. According to Fig. 2, the abnormal phenomena appear in the Tafel plot in the pressure range from 10 to 40 MPa and potential range from −0.8 to −1.1 V_{SSE}. The absolute value of the cathodic current decreases with decreasing cathodic potential. This tendency is different from that of the Tafel plot below 0.1 MPa.

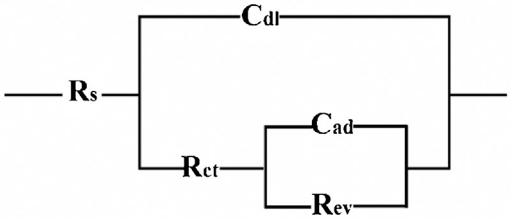

Fig. 1. The electrical equivalent circuit of the HER.

4.2. Hydrogen permeation measurements

To illustrate the abnormal phenomena in the Tafel plot under relatively high pressure, cathodic potentials in the abnormal potential region (-1.0 and −1.1 V_{SSE}) and below the abnormal potential region (-1.2 and −1.3 V_{SSE}) were applied on the hydrogen entry side during the hydrogen permeation tests. The permeation curves under various hydrostatic pressures and cathodic potentials at 25 °C are shown in Fig. 3(a)–(d). The connection between the apparent diffusivity D_C, which is obtained using the time lag method [8], and hydrostatic pressure as well as the steady-state current density i_∞ and the hydrostatic pressure are shown in Fig. 4.

As seen in Fig. 4(a), i_∞ increases with hydrostatic pressure, which has been proven previously [9–11,37]. By using the single factor analysis model (SFAM) [38], the analysis of the relation between the hydrostatic pressure and the apparent diffusivity, D_C was performed. The rejection region, F, was calculated as

$$F = \frac{S_A/f_A}{S_e/f_e} \tag{27}$$

Where S_A and S_e are the quadratic sum of the standard deviations of the factor A and the error e, respectively. The variables f_A and f_e

Table 1
Fitting results from potentiodynamic polarization curves.

Pressure MPa	E_{eq} V_{SSE}	j^0 10^{-7} A cm^{-2}	β_c V dec^{-1}	α
0.1	−0.329	1.34	0.134	0.438
10	−0.243	1.64	0.127	0.465
20	−0.220	1.93	0.116	0.511
30	−0.211	2.40	0.119	0.498
40	−0.183	3.28	0.115	0.514

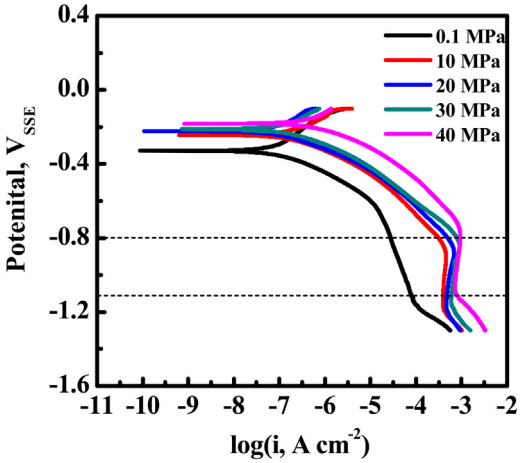

Fig. 2. Potentiodynamic polarization measurements under different hydrostatic pressures in 0.2 mol/L NaOH at 25 °C (scan rate: 0.33 mV/s, scan range: −0.1 to −1.3 V_{SSE}). Dashed lines represent the potential region with abnormal phenomena.

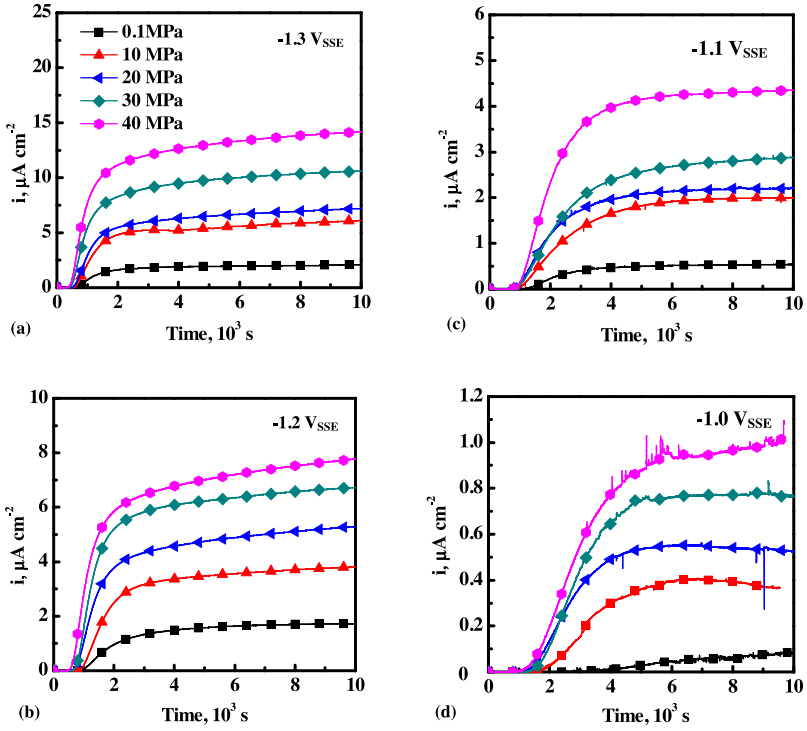

Fig. 3. Permeation curves under various hydrostatic pressure and cathodic potential at 25 °C.

are the degrees of freedom of the factor A and the error e, respectively.

The data for hydrostatic pressure less than 10 MPa and higher than 30 MPa are listed in Table 2. All of these data were divided into two groups. Group I contains the data for D_C at −1.0 and −1.1 V_{SSE}, and group II contains the data of D_C at −1.2 and −1.3 V_{SSE}.

As seen in Table 2, the factor A is the hydrostatic pressure. For group I (relatively high cathodic potential), the error square sum is $S_e = \sum_{i=1}^{2}\sum_{j=1}^{4}(D_{ij} - \overline{D}_i)^2 = 0.85$, the total declination square sum is $S_T = \sum_{i=1}^{2}\sum_{j=1}^{4}(D_{ij} - \overline{D})^2 = 0.97$, and the declination square sum for the hydrostatic pressure is $S_A = S_T - S_e = 0.12$. The degrees of freedom are $f_T = 7$, $f_A = 1$, and $f_e = 6$. Thus, $F_I = 0.87$ based on Eq. (27). Similarly, for group II (relatively low cathodic potential), $F_{II} = 4.39$, $F_{0.05}(1,6) = 5.99$ (95%) and $F_{0.01}(1,6) = 13.74$ (99%). Since F_I and F_{II} are less than $F_{0.05}$, it has little influence on D_C. However, compared to group I, the effect of the pressure on D_C is much more significant in group II. This phenomenon can be clearly seen in Fig. 4(b). Under the cathodic potential of −1.0 and −1.1 V_{SSE}, D_C is irregular with the change in the hydrostatic pressure, but it increases slightly with the hydrostatic pressure under −1.2 and −1.3 V_{SSE}.

4.3. EIS analysis

The EIS analysis was performed at 0.1 to 40 MPa and −1.0 to −1.2 V_{SSE}. The Nyquist and Bode plots are shown in Fig. 5. The fitting results, shown as solid lines in Fig. 5, were obtained using the electric equivalent circuit in Fig. 1. A constant phase angle element (CPE) is applied to substitute the double layer capacitance. The CPE can illustrate the non-ideal behavior of the capacitive elements caused by different physical phenomena. The values of the fitting results are listed in Table 3.

As shown in Fig. 5, the impendence absolute value of the experimental system decreases with hydrostatic pressure, and this tendency is more significant under relatively low cathodic potentials.

5. Discussion

5.1. Hydrostatic pressure effects on the HER kinetic parameters

Assuming that the rates of reactions (1)–(3) have exponential dependence on the potential [15,23], the corresponding reaction

Table 2
Apparent diffusivity D_C for low and high hydrostatic pressure.

Group	Pressure range	D_{ij} 10^{-6} cm^2 s^{-1}				$\overline{D}_i$ 10^{-6} cm^2 s^{-1}	$\overline{D}$ 10^{-6} cm^2 s^{-1}
I		−1.0 V_{SSE}		−1.1 V_{SSE}			
	≤10 MPa	0.60	1.25	1.65	1.49	1.25	1.37
	≥30 MPa	1.31	1.28	1.54	1.85	1.50	
II		−1.2 V_{SSE}		−1.3 V_{SSE}			
	≤10 MPa	2.06	2.16	2.88	2.93	2.51	2.83
	≥30 MPa	2.75	2.87	3.39	3.63	3.16	

rates are:

$$v_1 = k_1(1-\theta)\exp\left(\frac{-\alpha F\eta}{RT}\right) - k_{-1}\theta\exp\left(\frac{(1-\alpha)F\eta}{RT}\right) \quad (28)$$

$$v_2 = k_2\theta\exp\left(\frac{-\alpha F\eta}{RT}\right) - k_{-2}(1-\theta)P_{H_2}^{1/2} \quad (29)$$

$$v_3 = k_3\theta^2 - k_{-3}(1-\theta)^2 P_{H_2} \quad (30)$$

Where k_i and k_{-i} are the kinetic parameters of the forward and reverse reaction (i), α is the transfer coefficient, η is the over potential, and R and T have their usual meanings.

Since Bai proposed that unless $k_{-3} > k_3$, $k_{-2} > k_2$, k_{-3} and k_{-2} have no significant influence on the simulations, the reverse reaction rate in Eq. (29) and Eq. (30) can be ignored for mathematical simplicity [15]. By substituting Eq. (28), (29), and (30) into Eqs. (20), (21), and (22), one can get the relations between kinetic parameters (k_1, k_2, k_3, k_{-1}) and R_{ct}, R_0, τ. Here, we defined these relationships as $f_{R_{ct}} f_{R_0}$, and f_τ.

The value of τ, R_{ct} and R_0 can be obtained from Eq. (20), (23), (24) and Table 3. Since the variance of τ (σ_τ^2) is much smaller than R_{ct} and R_0, the weighted least-squares method is used in the calculation. The objective function for minimizing the error between $f_{R_{ct}} f_{R_0} f_\tau$ and R_{ct}, R_0, R_τ, which is calculated based on Table 3, Eq. (23) and (24) is:

$$f_e = \frac{1}{\sigma_{R_{ct}}^2}(f_{R_{ct}} - R_{ct})^2 + \frac{1}{\sigma_{R_0}^2}\left(f_{R_0} - R_0\right)^2 + \frac{1}{\sigma_\tau^2}(f_\tau - R_\tau)^2 \quad (31)$$

There are constraints for the kinetic parameters in Eq. (31). The kinetic parameters should fetch values from the (0,1) region. The kinetic parameters in $f_{R_{ct}} f_{R_0} f_\tau$ should enable f_e to achieve the global minimum under relative constraints.

Since the entry of hydrogen atoms into the bulk metal is very rare and most of these atoms recombine into hydrogen molecules via the HER, reactions (4) and (5) can be ignored, and Eq. (8) can be simplified to Eq. (32) when hydrogen permeation reaches the steady state:

$$v_1 - v_2 - 2v_3 = 0 \quad (32)$$

Combining Eq. (32) with Eq. (28) into Eq. (30), the mathematical expression for the hydrogen surface coverage θ can be written

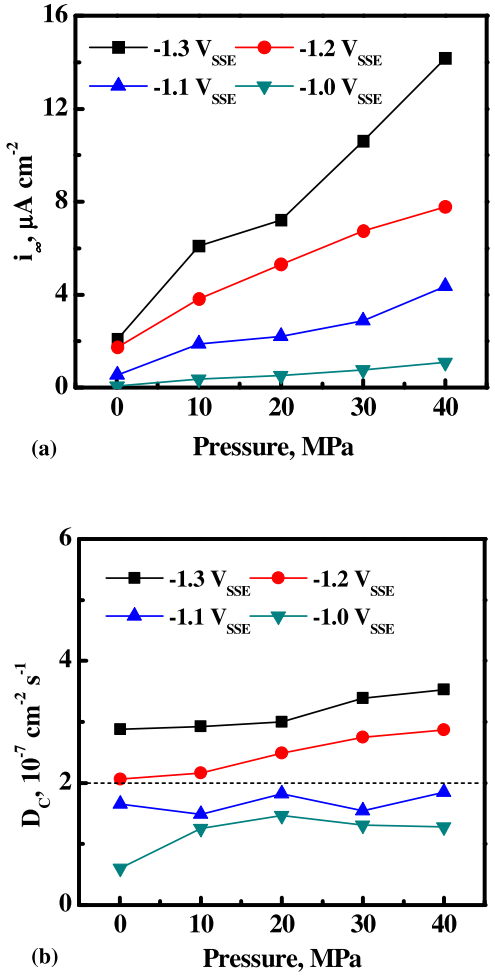

Fig. 4. Variations of the steady state current density i_∞ (a) and the apparent diffusivity D_C (b) as functions of the hydrostatic pressure and cathodic potential, the dashed line separates the cathodic potential region in (b).

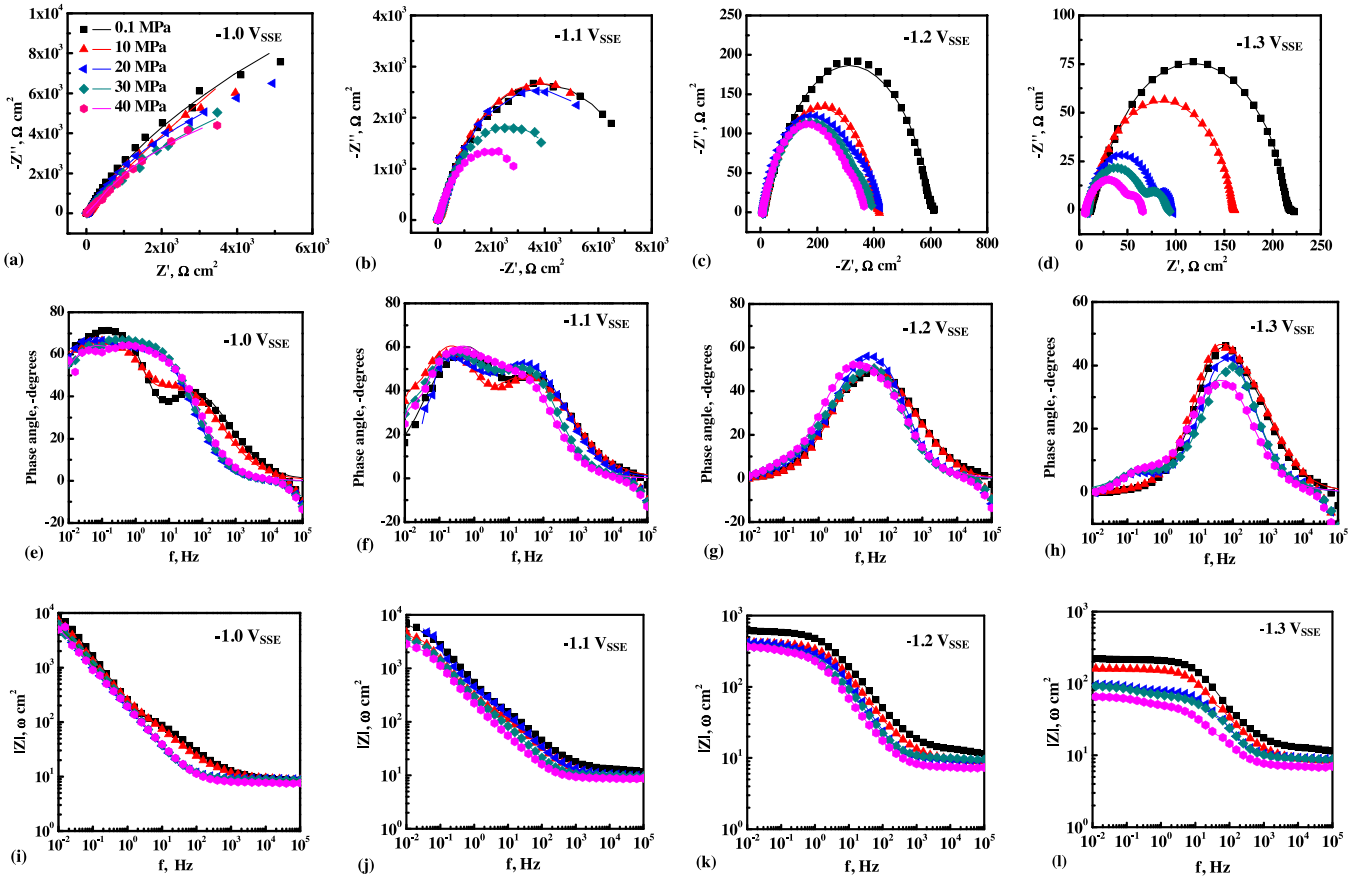

Fig. 5. EIS analysis results under different hydrostatic pressures and cathodic potentials at 25 °C: ((a)–(d) the Nyquist plots, (e)–(h) the Bode plots; (i)–(l) Modulus of impedance. Points are experimental data, while solid lines are fitting results.

Table 3
Values of the elements from the equivalent circuit in Fig. 1.

Potential V_{SSE}	Pressure MPa	η V	R_s Ωcm^2	R_{ct} Ω cm^2	C_{dl} 10^{-4} S cm^{-2} s^n	n	R_{ev} Ω cm^2	$C_{ad} \times 10^{-4}$ F cm^{-2}
	0.1	−0.67	12.17	2010.00	7.72	0.79	1.69×10^5	2.81
	10	−0.76	8.78	1751.10	8.90	0.81	5.31×10^4	4.12
−1.0	20	−0.78	9.25	1897.92	11.99	0.82	2.07×10^4	3.41
	30	−0.79	8.91	1915.56	11.75	0.80	2.25×10^4	1.16
	40	−0.82	7.61	1807.45	12.38	0.85	1.49×10^4	3.35
	0.1	−0.77	11.86	589.20	3.78	0.79	8.84×10^3	0.95
	10	−0.86	8.72	449.80	5.28	0.81	7.76×10^3	3.82
−1.1	20	−0.88	9.98	500.99	5.59	0.80	6.20×10^3	2.88
	30	−0.89	9.48	526.92	6.02	0.81	4.57×10^3	3.70
	40	−0.98	8.63	416.46	8.64	0.83	3.44×10^3	3.11
	0.1	−0.87	12.14	250.31	1.88	0.79	340.32	0.17
	10	−0.96	9.26	210.44	0.33	0.82	279.17	2.81
−1.2	20	−0.98	9.21	200.87	2.61	0.81	90.17	13.21
	30	−0.99	9.74	180.45	2.67	0.80	41.37	12.56
	40	−1.08	7.25	118.60	6.13	0.86	25.61	11.22
	0.1	−0.97	12.17	66.44	1.33	0.79	139.6	0.22
	10	−1.06	8.66	48.29	1.63	0.80	103.20	0.32
−1.3	20	−1.08	9.25	50.32	2.12	0.81	15.66	52.14
	30	−1.09	8.87	48.06	2.48	0.81	19.87	22.61
	40	−1.18	6.91	45.98	7.45	0.81	11.77	18.19

as:

$$\theta = -\frac{1}{4k_3}\left(k_1 e^{-\frac{\alpha F\eta}{RT}} + k_2 e^{-\frac{\alpha F\eta}{RT}} + k_{-1} e^{\frac{(1-\alpha)F\eta}{RT}}\right) + \frac{1}{4k_3}\left(\left(k_{-1} e^{\frac{(1-\alpha)F\eta}{RT}}\right)^2 + 2k_1 k_{-1} e^{\frac{(1-\alpha)F\eta}{RT}} e^{-\frac{\alpha F\eta}{RT}} + 2k_2 k_{-1} e^{\frac{(1-\alpha)F\eta}{RT}} e^{-\frac{\alpha F\eta}{RT}} + \left(k_1 e^{-\frac{\alpha F\eta}{RT}}\right)^2 + 2\left(e^{-\frac{\alpha F\eta}{RT}}\right)^2 k_1 k_2 + \left(k_2 e^{-\frac{\alpha F\eta}{RT}}\right)^2 + 8k_3 k_1 e^{-\frac{\alpha F\eta}{RT}}\right)^{1/2} \quad (33)$$

Once the kinetic parameters are obtained, θ can be obtained from Eq. (33). The kinetic parameters and θ are listed in Table 4. The results in Table 4 are also shown in Figs. 6 and 7. As seen in Fig. 6, k_1 and k_{-1} increase with hydrostatic pressure, which means that both the forward and the reverse Volmer reactions are accelerated with hydrostatic pressure. Based on Eq. (28), the forward reaction rate of the Volmer reaction is much faster than the reverse reaction rate in the applied cathodic potential region. Thus, the reaction rate of the Volmer reaction increases with hydrostatic pressure, which means that the amount of adsorbed hydrogen atoms increases with hydrostatic pressure. On the other hand, k_2 increases with hydrostatic pressure, indicating that the reaction rate of the Heyrovsky reaction increases with hydrostatic pressure, which causes the number of adsorbed hydrogen atoms to decrease with hydrostatic pressure. Fig. 6 also shows that k_3 decreases with hydrostatic pressure, which means that the reaction rate of the Tafel recombination decreases with hydrostatic pressure, increasing the number of adsorbed hydrogen atoms with hydrostatic pressure.

Fig. 7 shows that the hydrogen surface coverage decreases as the cathodic potential decreases at 40 MPa and −1.2 and −1.3 V_{SSE}. This phenomenon indicates that the hydrostatic pressure increases the Heyrovsky reaction rate, which dominates the entire process. Thus, hydrogen surface coverage decreases. On the other hand, at 0.1 MPa, hydrogen surface coverage increases dramatically with decreasing cathodic potential. However, this tendency is not significant at relatively high hydrostatic pressure, which indicates that absorbed hydrogen atoms saturate vacancies on the surface of the metal more quickly at relatively high pressure as the cathodic potential decreases.

5.2. Abnormal Tafel plot phenomena under hydrostatic pressure

Electrons take part in reactions (1) and (2), thus, the current of the Tafel plot under the hydrogen evolution potential in Fig. 2 can be represented as:

$$i = -F(v_1 + v_2) \quad (34)$$

Combining Eq. (32) with Eq. (34), the current can also be written as:

$$i = -2F(v_2 + v_3) \quad (35)$$

It can be seen that the absolute value of i decreases with decreasing cathodic potential in the 10 to 40 MPa pressure range, and −0.8 to −1.1 V_{SSE} potential range. As assumed in the section 5.1, the rates of reactions (1) through (3) have exponential dependence on the potential, which means that the kinetic parameters k_2, k_{-2}, k_3 and k_{-3} are independent of the cathodic potential. By combining Eqs. (29) and (30) with Eq. (35), one can see that the only factor decreasing the absolute value of i is hydrogen partial pressure (P_{H_2}). Hydrogen partial pressure increases the reaction rates of reverse reactions (2) and (3). Actually, P_{H_2} on the hydrogen entry side of the specimens is affected by hydrogen solubility. Hydrogen solubility in electrolyte increases with hydrostatic pressure [39]. Hydrogen molecules are dissolved in the electrolyte and are gathered near the entry side of the membrane, which could increase P_{H_2} and restrain adsorbed hydrogen atoms combining into H_2 molecules through the Tafel reaction (3). Compared with 0.1 MPa, P_{H_2} is larger at relatively high hydrostatic pressure. P_{H_2} also increases as the cathodic potential decreases and reaches a stable state at a critical point. Based on this assumption, k_{-2} and k_{-3} are independent of the cathodic potential. As the cathodic potential decreases, θ becomes stable very quickly under high pressure based on Fig. 7. Thus, according to Eq. (29) and (30), high P_{H_2} increases the reaction rates of reverse reactions (2) and (3) at high pressure as the cathodic potential decreases.

On the other hand, the reaction rates of forward reactions (2) and (3) increase as the cathodic potential decreases, based on the calculation result of Eq. (29) and (30).

It can be concluded that at the cathodic potentials of −1.0 and −1.1 V_{SSE}, the reaction rates of reverse reactions (2) and (3) dominate, and P_{H_2} increases as the cathodic potential decreases. The reverse reaction rate increases, and the total reaction rates v_2 and v_3 decrease, which causes the current to decrease as the cathodic potential decreases at relatively high pressures, as indicated by Eq. (35). Under the cathodic potentials of −1.2 and −1.3 V_{SSE}, the forward reaction rate, controlled by the charge transfer, dominates, causing the current to increase as the cathodic potential decreases.

5.3. Hydrogen adsorption transformation conditions with hydrostatic pressure

The Faradaic resistance of the reaction system can be represented by the sum $R_{ct} + R_{ev}$ under the same cathodic potential. It is related to the kinetic parameters of the HER. In the cathodic

Table 4
Kinetic parameters and hydrogen surface coverage at various pressure.

Kinetic parameters					
k mol cm^{-2} s^{-1}	0.1 MPa	10 MPa	20 MPa	30 MPa	40 MPa
$k_1 \times 10^{15}$	5.89	6.46	6.81	19.89	19.81
$k_2 \times 10^{18}$	1.01	1.20	2.65	18.91	18.88
$k_3 \times 10^{10}$	4.76	4.39	2.80	2.03	2.06
$k_{-1} \times 10^{15}$	3.24	12.28	17.19	19.89	19.80
Hydrogen surface coverage					
Potential V_{SSE}	0.1 MPa	10 MPa	20 MPa	30 MPa	40 MPa
−1.0	0.526	0.927	0.985	0.994	0.997
−1.1	0.801	0.987	0.998	0.998	0.999
−1.2	0.949	0.998	0.999	0.999	0.999
−1.3	0.990	0.998	0.999	0.999	0.998

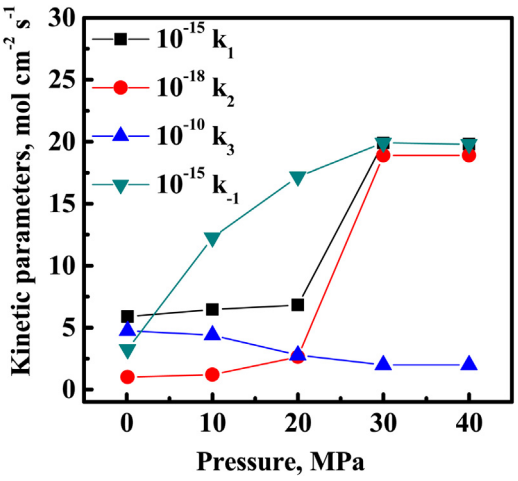

Fig. 6. Relationships between the kinetic parameters and the hydrostatic pressure.

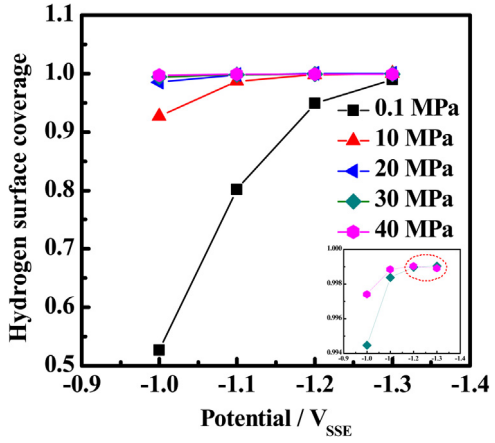

Fig. 7. Relationships between hydrogen surface coverage, cathodic potential and hydrostatic pressure. The part in the dashed oval means that the hydrogen surface coverage decreases with decreasing cathodic potential under the potential region from −1.2 to −1.3 V_{SSE} at 40 MPa.

potential region (-1.2 to −1.3 V_{SSE}), the HER is controlled by the charge transfer, as mentioned above. The cathodic potential *E vs.* log[1/(R_{ct} + R_{ev})] plot should be linear, and it should have the same slope as the Tafel plot [15,40]. Fig. 8 shows this plot for the A514 steel in NaOH under each hydrostatic pressure along with the Tafel plot at 0.1 MPa and the considered potential region (-1.0 to −1.3 V_{SSE}) obtained from Fig. 2. The slope of the Tafel plot and the simulated *E vs.* log[1/(R_{ct} + R_{ev})] plot are almost the same under the cathodic potential region (-1.2 to −1.3 V_{SSE}). The observed separations are 1.19, 1.27, 1.5, 1.61, and 1.8 at each hydrostatic pressure.

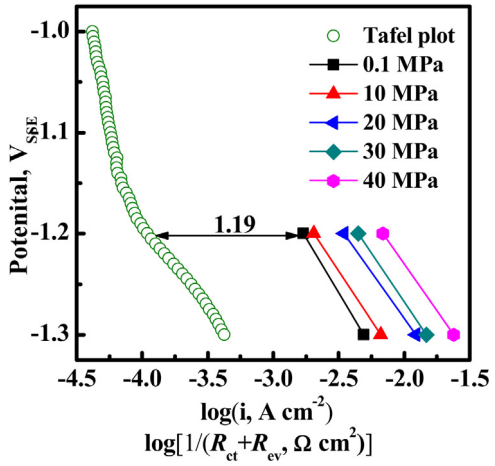

Fig. 8. Experimental Tafel plot (circles) and simulated *E vs.* log[1/(R_{ct} + R_{ev})] plot (solid points) for the HER on A514 steel in 0.2 mol/L NaOH solution at 25 °C.

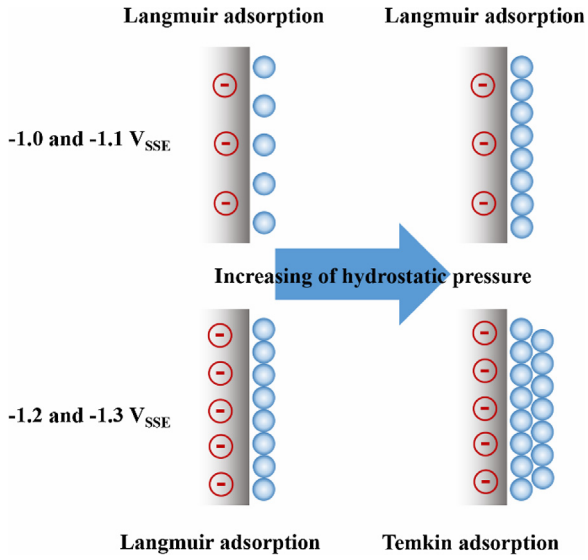

Fig. 9. Pressure effect on the Langmuir adsorption under high potential and multilayer adsorption under low potential.

Bai et al. mentioned that the Tafel slope can be represented as $di/d\eta = -(\alpha F/RT)i$. At high over-potential and zero frequency, the Faradic admittance was shown as $(\partial i/\partial\eta)_{\omega=0} = (Y_f)_{\omega=0} = 1/(R_{ct} + R_{ev})$. Combining these two equations, $\log(R_{ct} + R_{ev})^{-1} = \log(-i) + \log\alpha F/RT$. Thus, the theoretical separation between the cathodic potential E *vs.* $\log[1/(R_{ct} + R_{ev})]$ plot and the Tafel plot for the Langmuir monolayer absorption is equal to $\log(\alpha F/RT)$ [15]. For $\alpha = 0.438$ and T = 298 K, $\log(\alpha F/RT) = 1.23$, which is close to the experimental value obtained at 0.1 MPa. According to the Bai's theory, it was derived from the Langmuir isotherm [41]. Once the Langmuir hydrogen adsorption condition changes, the Temkin adsorption isotherm should be used. Thus the value of $\log[1/(R_{ct} + R_{ev})]$ changes. This change is represented as the term of A on the right side of Eq. (15) in ref. [15], which is shown as $\log(R_{ct} + R_{ev})^{-1} = \log(-i) + \log\alpha F/RT + A$. The separation of 1.8 found in the experiments at 40 MPa indicated the Temkin adsorption condition, and the theoretical separation of the Temkin adsorption is 1.86 [15]. This experimental evidence indicates hydrogen adsorption condition transfer from the Langmuir monolayer adsorption at 0.1 MPa to the Temkin adsorption at 40 MPa. This behavior could be due to the effects of the pressure on the rates of reactions (1) through (3).

5.4. Cathodic potential and pressure effects on the apparent diffusivity D_C

As shown in Fig. 7, θ increases dramatically with hydrostatic pressure from 0.52 to 0.99 at −1.0 V$_{SSE}$. However, the increment of θ from 0.1 MPa to 40 MPa decreases at lower cathodic potential, which indicates that at relatively high cathodic potentials (-1.0 and −1.1 V$_{SSE}$), the adsorbed hydrogen atoms saturate vacancies on the hydrogen charging side caused by the increasing hydrostatic pressure. This is the Langmuir monolayer adsorption. At relatively low cathodic potentials (-1.2 and −1.3 V$_{SSE}$), vacancies on the hydrogen charging side are saturated at 0.1 MPa and tend to be the Temkin adsorption at high pressures, as shown in Fig. 8. This phenomenon is schematically shown in Fig. 9.

Based on Fig. 4 (b), D_C increase with hydrostatic pressure more obvious at −1.2 and −1.3 V$_{SSE}$ potentials than at −1.0 and −1.1 V$_{SSE}$ potentials, indicating that the multilayer Temkin adsorption increases the apparent diffusivity. In contrast, the increase in θ under the Langmuir adsorption does not affect D_C.

6. Conclusions

In this paper, hydrostatic pressure-induced coupling mechanism is demonstrated. Hydrostatic pressure increases the Volmer reaction rate by increasing the absolute value of the cathodic overpotential and the kinetic parameters k_1 and k_{-1}. It decreases the Tafel recombination rate by increasing the solubility of H_2 in the electrolyte and decreasing the kinetic parameter k_3. These two effects increase the amount of adsorbed hydrogen atoms with hydrostatic pressure. On the other hand, pressure increases the Heyrovsky reaction rate by increasing the absolute value of the cathodic overpotential and the kinetic parameter k_2, which decreases the amount of adsorbed hydrogen atoms with hydrostatic pressure.

The hydrogen adsorption condition with applied cathodic potentials of −1.0 and −1.1 V$_{SSE}$ is by the Langmuir monolayer adsorption at every pressure. However, the adsorption condition transforms from the Langmuir monolayer adsorption to the Temkin adsorption with hydrostatic pressure under applied cathodic potentials of −1.2 and −1.3 V$_{SSE}$. The change in the adsorption condition affects the apparent diffusivity of hydrogen permeation more significantly than the Langmuir monolayer adsorption.

At pressure ranged from 10 to 40 MPa, the Tafel recombination and the Heyrovsky reaction are controlled by the P_{H_2} in the electrolyte in the potential region of −1.0 and −1.1 V$_{SSE}$. However, the entire HER process is controlled by the cathodic potential in the potential region of −1.2 and −1.3 V$_{SSE}$.

Acknowledgements

This project was supported by the National Nature Science Foundation of China under grant No. 51371035 and the National Basic Research Program of China under grant No. 2014CB643301. AV acknowledges support from the National Science Foundation under the IRES 1358088 grant.

References

[1] D. Festy, Cathodic protection of steel in deep sea hydrogen embrittlement risk and cathodic protection criteria, Corrosion 01011 (2001).
[2] P. Pohjanne, D. Festy, Hydrogen embrittlement of duplex stainless steel and maraging steel in sea water: Effect of pressure, NACE International (1994).
[3] W.H. Thomason, K.P. Fischer, Cathodic protection of steel structures in deep water: A review, Offshore Technology Conference (1991).
[4] F.W.H. Dean, S.W. Powell, B. Muckherjee, C.M. Fowler, The effect of pressure on hydrogen charging of carbon steel under cathodic protection, NACE International (2008).
[5] S.M. Hesjevik, Hydrogen embrittlement from cathodic protection on supermartensitic Stainless steel -Case history, Corrosion 04545 (2004).
[6] T.S. Taylor, R.Bird T.Pendlington, Foinaven super duplex materials cracking investigation, Offshore Technology Conference 10965 (1999).
[7] S. Olsen, S.M. Hesjevik, Hydrogen embrittlement from CP on supermartensitic stainless steels – recommendations for new qualification methods, Corrosion 04546 (2004).
[8] M.A.V. Devanathan, Z. Stachurski, The mechanism of hydrogen evolution on iron in acid solutions by determination of permeation rates, J. Electrochem. Soc. 111 (1964) 619–623.
[9] L. Nanis, J.J. DeLuccia, Effects of hydrostatic pressures on electrolytic hydrogen in iron, ASTM STP. 445 (1969) 55–67.
[10] J. Woodward, R.P.M. Procter, The effect of hydrostatic pressure on hydrogen permeation and embrittlement of structural steels in seawater, Conference Proceedings (1996) 253–267.
[11] R.F. Blundy, L.L. Shreir, The effect of pressure on the permeation of hydrogen through steel, Corros. Sci. 17 (1977) 509–527.
[12] A. Smirnova, R. Johnsen, Influence of temperature and hydrostatic pressure on hydrogen diffusivity and permeability in 13%cr super martensitic stainless steel under cathodic protection, Corrosion 10292 (2010).
[13] T.Y. Zhang, Y.P. Zheng, Effects of absorption and desorption on hydrogen permeation—I. Theoretical modeling and room temperature verification, Acta Mater. 46 (1998) 5023–5033.
[14] X.L. Xiong, X. Tao, Q.J. Zhou, J.X. Li, A.A. Volinsky, Y.J. Su, Hydrostatic pressure effects on hydrogen permeation in A514 steel during galvanostatic hydrogen charging, Corros. Sci. 112 (2016) 86–93.
[15] L. Bai, D.A. Harrington, B.E. Conway, Behavior of overpotential—deposited species in Faradaic reactions—II. ac Impedance measurements on H_2 evolution kinetics at activated and unactivated Pt cathodes, Electrochim. Acta 32 (1987) 1713–1731.
[16] A. Lasia, Applications of Electrochemical Impedance Spectroscopy to Hydrogen Adsorption, Evolution and Absorption into Metals, in: B. Conway, R. White (Eds.), Modern Aspects of Electrochemistry, Springer, US, 2002, pp. 1–49.
[17] D.A. Harrington, B.E. Conway, AC impedance of Faradaic reactions involving electrosorbed intermediates—I. Kinetic theory, Electrochim. Acta 32 (1987) 1703–1712.
[18] G. Zheng, B.N. Popov, R.E. White, Hydrogen-atom direct-entry mechanism into metal membranes, J. Electrochem. Soc. 142 (1995).
[19] I. Bagotskaya, Effect of the solution composition on the diffusion rate of electrolytic hydrogen through metallic diaphragms .1. diffusion of hydrogen through iron diaphragms, Zhurnal Fizicheskoi Khimii 36 (1962).
[20] C. Lim, S.-I.I. Pyun, Impedance analysis of hydrogen absorption reaction on Pd membrane electrode in 0.1 M LiOH solution under permeable boundary conditions, Electrochim. Acta 39 (1994) 363–373.
[21] C. Gabrielli, G. Maurin, L. Mirkova, H. Perrot, Transfer function analysis of hydrogen permeation through a metallic membrane in a Devanathan cell: Part II: Experimental investigation on iron membrane, J. Electroanal. Chem. 590 (2006) 15–25.
[22] C. Gabrielli, G. Maurin, L. Mirkova, H. Perrot, B. Tribollet, Transfer function analysis of hydrogen permeation through a metallic membrane in a Devanathan cell. I. Theory, J. Electroanal. Chem. 590 (2006) 1–14.
[23] C. Lim, S.-I.I. Pyun, Theoretical approach to faradaic admittance of hydrogen absorption reaction on metal membrane electrode, Electrochim. Acta 38 (1993) 2645–2652.
[24] J.O.M. Bockris, J. McBreena, L. Nanis, The hydrogen evolution kinetics and hydrogen entry into α-iron, J. Electrochem. Soc. 112 (1965).
[25] N. Amokrane, C. Gabrielli, E. Ostermann, H. Perrot, Investigation of hydrogen adsorption-absorption on iron by EIS, Electrochim. Acta 53 (2007) 700–709.
[26] T. Zakroczymski, Adaptation of the electrochemical permeation technique for studying entry, transport and trapping of hydrogen in metals, Electrochim. Acta 51 (2006) 2261–2266.
[27] J. Svoboda, G. Mori, A. Prethaler, F.D. Fischer, Determination of trapping parameters and the chemical diffusion coefficient from hydrogen permeation experiments, Corros. Sci. 82 (2014) 93–100.
[28] J.J.M. Jebaraj, D.J. Morrison, I.I. Suni, Hydrogen diffusion coefficients through Inconel 718 in different metallurgical conditions, Corros. Sci. 80 (2014) 517–522.
[29] S.J. Kim, D.W. Yun, H.G. Jung, K.Y. Kim, Determination of hydrogen diffusion parameters of ferritic steel from electrochemical permeation measurement under tensile loads, J. Electrochem. Soc. 161 (2014) 173–181.
[30] M. Enyo, T. Maoka, The overpotential components on the palladium hydrogen electrode, J. Electroanal. Chem. 108 (1980) 277–292.
[31] P. Subramanyan, J. Bockris, B. Conway, E. Yeager, R. White, Comprehensive Treatise of Electrochemistry, 4(1981) , pp. 411.
[32] M.H.A. Elhamid, B.G. Ateya, H.W. Pickering, Determination of the rate constants of hydrogen absorption into metals, J. Electrochem. Soc. 147 (2000) 2959–2963.
[33] R.D. Armstrong, M. Henderson, Impedance plane display of a reaction with an adsorbed intermediate, J. Electroanal. Chem. 39 (1972) 81–90.
[34] C. Zhang, Z.W. Zhang, L. Liu, Degradation in pitting resistance of 316L stainless steel under hydrostatic pressure, Electrochim. Acta 210 (2016) 401–406.
[35] S. Sarkar, W. Aquino, Changes in electrodic reaction rates due to elastic stress and stress-induced surface patterns, Electrochim. Acta 111 (2013) 814–822.
[36] Y. Ogata, T. Sakka, M. Iwasaki, Diffusion through a multilayered phase in electrochemical systems: an approach by numerical inversion of the Laplace transform, J Appl Electrochem. 25 (1995) 41–47.
[37] X.L. Xiong, X. Tao, J.X. Li, Y.J. Su, Effect of hydrostatic pressure on hydrogen permeation in Armco iron with potentiostatic hydrogen charging, unpublished work, (2016) .
[38] H. Ma, C. Cui, X. Li, Z. Sun, Study of high performance autoclaved shell-aggregate from propylene oxide sludge, Constr. Build. Mater. 25 (2011) 3030–3037.
[39] E. Bender, U. Klein, W.P. Schmitt, J.M. Prausnitz, Thermodynamics of gas solubility: Relation between equation-of-state and activity-coefficient models, Fluid Phase Equilibr. 15 (1984) 241–255.
[40] E.A. Franceschini, G.I. Lacconi, H.R. Corti, Kinetics of the hydrogen evolution on nickel in alkaline solution: new insight from rotating disk electrode and impedance spectroscopy analysis, Electrochim. Acta 159 (2015) 210–218.
[41] A. Frumkin, B. Damaskin, J. Bockris, B. Conway, Modern Aspects of Electrochemistry, vol. 3, JOM Bockris Butterworth, London, 1964.